JOURNAL OF GEOPHYSICAL RESEARCH: PLANETS, VOL. 118, 2488–2501, doi:10.1002/2013JE004465, 2013

A radiative transfer model to simulate light scattering in a compact granular medium using a Monte-Carlo approach: Validation and first applications

C. Pilorget,[1,2] M. Vincendon,[1] and F. Poulet[1]

Received 18 June 2013; revised 21 September 2013; accepted 8 November 2013; published 12 December 2013.

[1] A new radiative transfer model to simulate light scattering in a compact granular medium using a Monte-Carlo approach is presented. The physical and compositional properties of the sample can be specified at the grain scale, thus allowing to simulate different kinds of heterogeneities/mixtures within the sample. The radiative transfer is then calculated using a ray tracing approach between the grains, and probabilistic physical parameters such as a single scattering albedo and a phase function at the grain level. The reflectance and the albedo can be computed at different scales and for different geometries: from the grain scale to the sample one. The photometric behavior of the model is validated by comparing the bidirectional reflectance obtained for various media and geometries with the one of semi-infinite multilayer models, and a few first applications are presented. This model will be used to refine our understanding of visible/NIR remote sensing data of planetary surfaces, as well as future measurements of hyperspectral microscopes which may be able to resolve spatial compositional heterogeneities within a given sample.

Citation: Pilorget, C., M. Vincendon, and F. Poulet (2013), A radiative transfer model to simulate light scattering in a compact granular medium using a Monte-Carlo approach: Validation and first applications, *J. Geophys. Res. Planets*, *118*, 2488–2501, doi:10.1002/2013JE004465.

1. Introduction

[2] As solar light penetrates into the surface, it is partially reflected back by interaction with its constituents and structures. The angular distribution of this signal, as well as its evolution with the light wavelength give essential information about the physical and compositional properties of this surface. With the common use of spectroscopic techniques from orbit, radiative transfer models simulating the interaction of light with planetary surfaces are essential tools to characterize these properties.

[3] Within planetary surfaces, solar light is subjected to five basic mechanisms: scattering by subwavelength and wavelength size materials, absorption, diffraction, reflection, and refraction, taking place inside various and numerous structures encountered or at their optical interfaces. These interfaces could present complex and irregular shapes at different geometric scales. Approximate solutions to the problem of propagation of electromagnetic radiation through these disordered media can be obtained [*de Haan et al.*, 1987; *Stamnes et al.*, 1988; *Grenfell*, 1991; *Peltoniemi*, 1993; *Hapke*, 1993]. Among them, Monte-Carlo approaches, doubling and multistream methods can be considered according to the type of medium, the required outputs and the computing time.

[4] Most of the models currently used to simulate the spectroscopic and photometric behaviors of planetary surfaces represent the surface as a semi-infinite plane-parallel multilayer medium [*Hapke*, 1993; *Douté and Schmitt*, 1998; *Shkuratov et al.*, 1999]. These models use mean scattering and absorption properties for each layer (that can be considered as a single grain as for the Shkuratov' model). During its transfer within the medium, the light is not sensitive to the discrete spatial distribution of the structures but only to their local mean properties. These fast-computing models have proved to be rather efficient to simulate both qualitatively and quantitatively remote sensing data from the Moon, asteroids, satellites and planets [e.g., *Johnson and Grundy*, 2001; *Cruikshank and Dalle Ore*, 2003; *Cruikshank et al.*, 2005; *Denevi et al.*, 2008; *Poulet et al.*, 2002, 2009]. Some limitations have nevertheless been highlighted [*Shepard and Helfenstein*, 2007, 2011; *Shkuratov et al.*, 2012]. Moreover, they cannot model observations containing spatial resolved heterogeneities.

[5] In the approximation of geometric optics, which can be applied in the visible and near-infrared spectral ranges ($\approx$ 0.4–2.5 μm) for the typical size range of grains/structures we deal with (typically 10 μm to a few mm), ray-tracing methods based on Monte-Carlo approaches can also be used.

[1]Institut d'Astrophysique Spatiale, Universite de Paris Sud 11, Orsay, France.
[2]Division of Geological and Planetary Sciences, Caltech, Pasadena, California, USA.

Corresponding author: C. Pilorget, Division of Geological and Planetary Sciences, Caltech, Pasadena, CA 91125, USA. (cpilorge@caltech.edu)

2169-9097/13/10.1002/2013JE004465

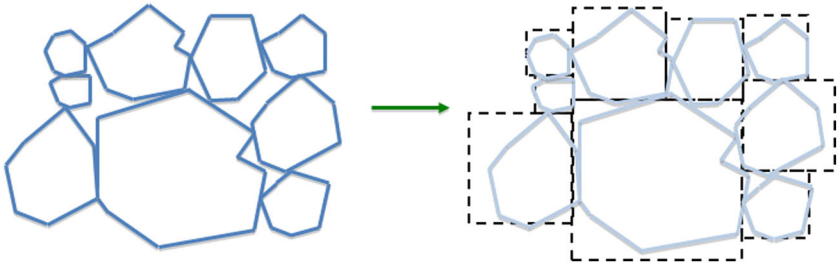

Figure 1. Example of the modeling of a compact granular sample with a given grain size distribution. Each grain is associated with a cube of the corresponding size.

This method is however far more time-consuming that semi-analytical models. The Monte-Carlo approach has been used for instance to compute the scattering properties of individual complex-shaped particles [*Bottlinger and Umhauer*, 1991; *Muinonen et al.*, 1996; *Hartman and Domingue*, 1998; *Grundy et al.*, 2000], to study specific photometric behaviors, such as the effect of porosity on the reflectance [*Peltoniemi and Lumme*, 1992; *Stankevich and Shkuratov*, 2004] or the unexpected backscattering properties of planetary surfaces [*Hillier*, 1997; *Hillier and Buratti*, 2001]. These models however are limited by complexity and time computation, thus generally limiting the medium to a few tens or hundreds of grains.

[6] A new radiative transfer model to simulate the light scattering in a compact granular medium, accounting for a few millions of grains, and using a Monte-Carlo approach, is presented here. The medium is defined by a given grain size distribution, and by optical properties that can be specific for each grain. The different grains are then set in a grid, allowing to create spatial heterogeneities at specific locations within the medium (e.g., a specific grain among other grains or different kinds of mixtures, such as linear, intimate, or layered). The radiative transfer is then calculated using a ray tracing approach between the grains, and probabilistic scattering parameters such as a single scattering albedo and a phase function at the grain level, thus leading to significantly faster computation times that classical ray tracing models.

2. Model Description

2.1. Introduction

[7] The model presented is a Monte-Carlo code, allowing to compute the radiative transfer within a compact granular medium. This latter can represent the soil of a planetary body or a powdered sample, for example. In the following sections, this compact granular medium is referred to as the "sample". The approximation of geometric optics is assumed. As the main applications of our interest concern the visible/near-infrared ranges (from 0.4 up to several micrometers depending on the thermal contribution of the planetary body), the model will be applied to samples made of grains whose size range typically from 10 to a few hundreds of μm.

[8] Since the approximation of geometric optics is assumed, the opposition effect present at low phase angles is only partially simulated. Indeed the opposition effect results from two different physical mechanisms: the Shadow Hiding Opposition Effect (SHOE) and the Coherent Backscatter Opposition Effect (CBOE). The SHOE, which takes the form of a broad small amplitude increase of the reflectance, is related to the shadowing of grains for certain geometries. The CBOE, which takes the form of a sharp intense peak, is related to the coherent combination of specific waves at low phase angle and is therefore not simulated here.

[9] The model, presented below, can be described in two steps: a first one generating the sample and a second one treating the interactions between the photons and the generated sample.

2.2. Sample Generation

2.2.1. Grains Positioning

[10] The sample generation is a particularly important step in the model. We attempt to model a sample that is the most representative of natural materials while avoiding to model precisely the grain shape and the positioning of each point of the grain, which would require a prohibitively high computation time. We therefore use here a method based on: (1) an accurate positioning of a given distribution of grains within a grid, as shown in Figure 1 and (2) a probabilistic approach to the irregular shape of the grains.

[11] In the approximation of geometric optics in the visible and near-infrared range, a grid step (which defines the smallest grain size of the sample) between 10 and 20 μm is typically used. All the grains that are generated have a grain size that is a multiple of this grid unit "GU", thus leading to grain sizes from 1 to S_{max} GU, with S_{max} the largest grain size (S_{max} = 20 or more typically).

[12] The grain size distribution on planetary surfaces generally remains poorly known. The Moon is probably the major exception since precise measurements have been obtained from the lunar samples that were brought back by Apollo astronauts [*McKay et al.*, 1974]. A few in situ data have also been obtained in the case of Mars [e.g., *Goetz et al.*, 2010]. The grain size distribution depends on various environmental factors, such as the impact rate at the surface of the planetary body and the different geological processes that the sample has experienced (leaching and other erosion processes, cryoclasty, etc.). Natural grain size distributions are nevertheless expected to follow typical lognormal or power laws [*Mishchenko et al.*, 2002]. In addition to a more realistic simulation of the surface soil of planetary bodies, using a grain size distribution limits the biases that can be encountered by using a monosize distribution. Finally, the wide particle size distribution (typically a variation of the grain size by a factor of 20) allows the use of small grains to

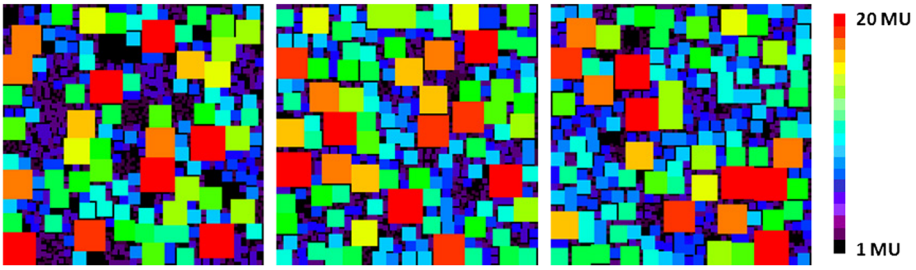

Figure 2. Cross section (x,y) of a sample that has been generated from a power law r^{-3} (S_{max} = 20 GU). This is a 200 × 200 × 100 GU grid. From left to right z = 1 (top of the sample), z = 39, and z = 69. A different color is associated with each grain size.

fill the vacated areas around the larger grains, as encountered in natural samples.

[13] In this model, the user only needs to specify the volumic distribution of the different grain sizes (or the massic distribution by taking into account the density of the different materials), and the program automatically computes the number of grains for each grain size that are necessary to be positioned within the specified grid. Thus, if one specifies a weight percentage of 10% of 10 GU grains in a 100 × 100 × 100 GU grid, 100 of these grains are set in the grid.

[14] Once the grain size distribution is specified, the program sets randomly the grains in the grid one by one, using the following algorithm:

[15] The grains that have a size ranging from 2 to S_{max} GU are first set in the grid:

[16] 1. We look for the largest remaining grain (p GU) that needs to be set.

[17] 2. We then generate a random position within the grid (three random integers x, y, and z are generated following a uniform distribution).

[18] 3. Since the grain will occupy a volume of $p \times p \times p$ boxes within the grid, one checks if the randomly drawn position allows to place the grain in the limit of available volume (all locations where the drawn position can fit are tested, from the top to the bottom ones).

[19] 4. If the grain can be set according to the conditions expressed in step 3, the volume of the grid where the grain is placed becomes occupied and we return to step 1.

[20] 5. If the grain cannot be set according to the conditions expressed in step 3, a new random position is drawn. While the grain is not set, this step is repeated until we reach n iterations. This number n, typically around 1000, results from a trade-off between computation time and optimization of placement in the grid after a series of tests. This avoids an infinite loop in the case there is no remaining free space for this grain size in the grid.

[21] At the end of this step is constructed a grid where a maximum of grains according to the specified distribution is set. Unoccupied boxes are then filled with grains with 1 GU size. Therefore, the grid is now completely filled and the final grain size lays between 1 and S_{max} GU, as illustrated in Figure 2.

[22] Since 1 GU grains are used to complete the grid, their percentage directly derives from the granulometric distribution of larger grains. To fit the specified sample granulometric distribution, is set an option allowing not to systematically fill the remaining gaps by 1 GU grains. A certain fraction of 1 GU grains filling is specified and for each position, a random number between 0 and 1 is drawn following a uniform distribution. If the drawn number is below the specified fraction, the grain is set, otherwise, the box remains unfilled. This option is not required for typical natural grain size distributions like power laws (e.g., r^{-3}, $r^{-3.5}$) which have a large fraction of small grains, but is particularly useful for distributions like lognormal laws.

[23] Figure 3 shows the efficiency of this algorithm to generate an homogeneous sample for different specified grain size distribution (power and lognormal laws). Results are shown for a 300 × 300 × 300 GU grid. For each tested case, the grain size distribution within 300 × 300 × 20 GU subdivisions of the grid fits well the assumed global grain size distribution. The small variations around the specified grain size distribution increase as the grain size increases because of the discrete nature of the grains within the grid, and of their lower number within the sample. The top layers, however, generally show a slight increase of the largest grains fraction, as can be seen on Figure 3 where the top 20 GU thick layer contains up to 50% more 18 to 20 GU grains (purple curve). On the contrary, the bottom layer (orange curve) shows a slight increase of the smallest grains (1 GU) fraction (typically up to 20%). These small biases are due to the way the algorithm tests if the grain can be set in a given location or not (as described previously). Since these biases are very limited, we use the same algorithm, which limits the number of tested positions and has the advantage of being computationally inexpensive.

[24] One of the main purposes of this model is to simulate heterogeneities in terms of grains properties within the sample. An option has therefore been added to allow the user to specify the grain properties (size, composition, and physical properties, see section 2.2.2) at specific locations for simulation (see section 4) or for future comparison with a suite of well characterized samples. The algorithm first places these grains, then the other grains are set following the different steps described previously.

2.2.2. Grains Properties

[25] After the sample generation, the second step consists of defining the scattering properties of each grain. We assign each grain with the following parameters:

[26] 1. A single scattering albedo ω, calculated according to the grain size and optical properties (that relate to the composition).

[27] 2. A phase function that may be either specified or randomly generated.

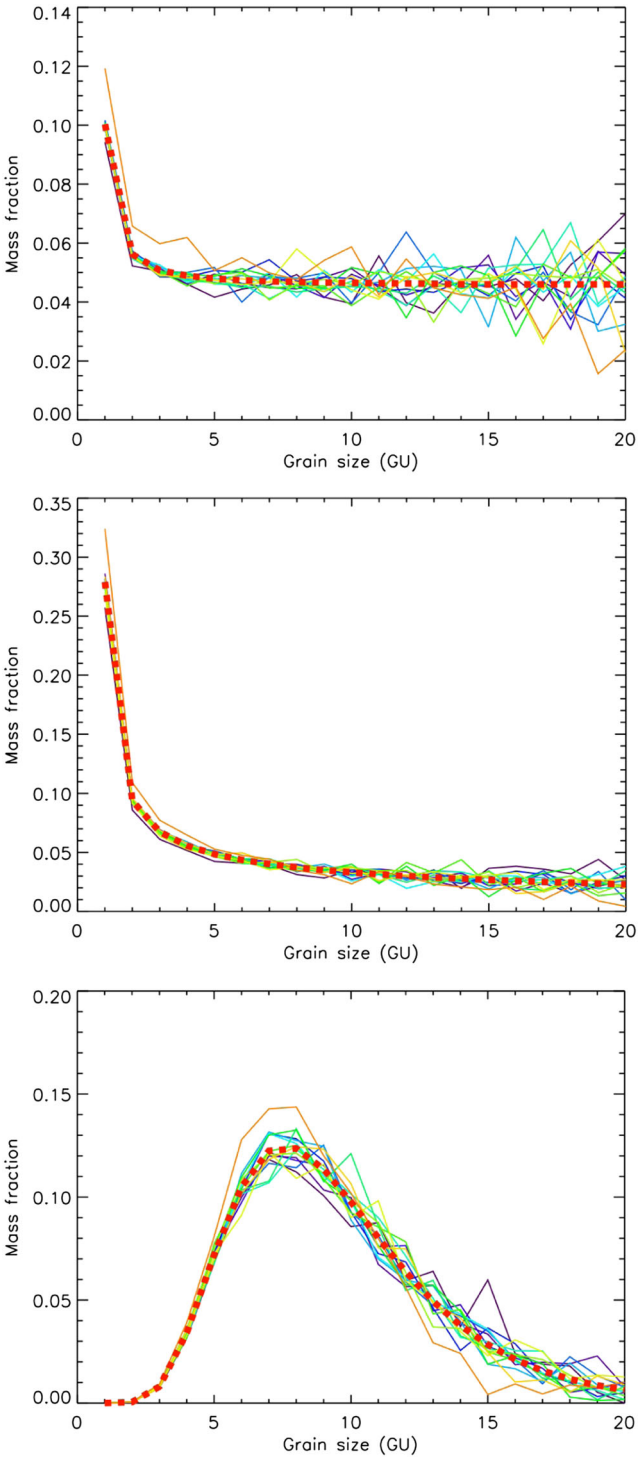

Figure 3. Comparison between different granulometric distributions generated by our algorithm and corresponding analytical law. (top) power law r^{-3}. (middle) power law $r^{-3.5}$. (bottom) Lognormal law. The generated samples use a 300 × 300 × 300 GU grid. For each 300 × 300 × 20 GU layer, the granulometric distribution is computed (thin colored continuous lines). The theoretical granulometric distribution has been added for comparison (thick dashed red line).

[28] This way, each grain can have its own specific properties if needed, to account for the variety of physical properties (grain shape, surface texture, and opacity) of the grains that may be found within a sample.

[29] Since the geometric optics is assumed, the diffraction peak of each particle taken individually can be neglected in the case of a compact granular medium [*Hapke*, 1993]. The single scattering albedo and phase functions that are used in this model can be thus calculated by removing this diffraction peak.

[30] *Single scattering albedo generation.* The single scattering albedo quantifies the probability of a photon that interacts with a grain to be absorbed. *Hapke* [1993] derived simple analytical expressions, only valid in geometric optics, that are used in the model to compute the single scattering albedo of each grain within the sample. The single scattering albedo is a function of the grain size, the complex optical index, the wavelength, and the potential existence of internal scatterers.

[31] *Phase function generation.* The phase function describes the angular distribution of light intensity scattered by a particle. In particular, the one lobe Henyey-Greenstein phase function, that is commonly used in photometry studies, has been implemented in the model. It can be expressed as follows:

$$p(\beta) = \frac{1 - g^2}{(1 - 2g\cos\beta + g^2)^{3/2}} \quad (1)$$

with $p(\beta)$ the probability of a photon to be scattered by a β angle: $\beta = 0°$ if the photon is scattered forward and $\beta = 180°$ if the photon is scattered backward. g is the asymmetry parameter: $g > 0$ for a forward scattering medium and $g < 0$ for a backward scattering one (see Figure 4).

[32] Other methods can also be used to compute the single scattering albedo and the phase function of the different grains with regards to their size, shape, and optical properties interparticulate distances [*Bottlinger and Umhauer*, 1991; *Muinonen et al.*, 1996; *Grundy et al.*, 2000; *Grynko and Shkuratov*, 2003].

[33] At the end of this second step, the sample is generated: each grain has a size that varies from 1 to S_{max} GU,

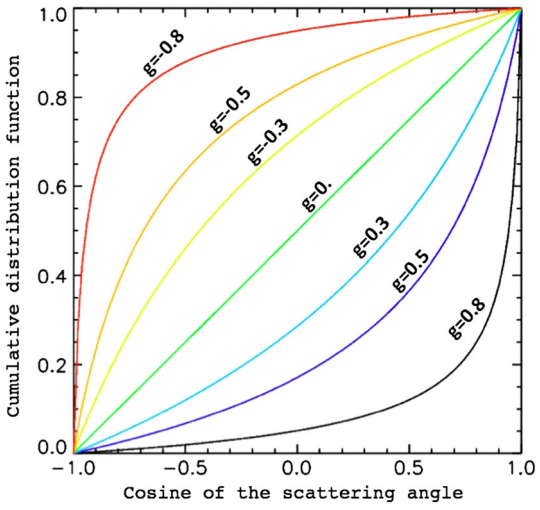

Figure 4. Cumulated distribution function for different one lobe Henyey-Greenstein phase functions.

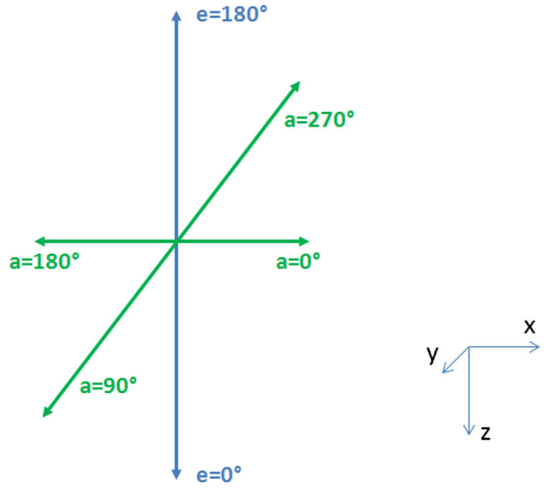

Figure 5. Conventions used in the model, regarding the elevation and azimuth angles.

is set at a certain location within the grid and has specific single scattering albedo and phase function.

2.3. Radiative Transfer Within the Sample

2.3.1. Photons Generation

[34] An orthonormal basis (O,x,y,z) is selected so that the incoming light reaches the sample at $z = 0$ (z is taken positive as we go down in the sample). To simulate a homogeneous illumination of the sample or part of the sample, the initial position of each photon is generated as follows:

[35] 1. The height relative to the sample z_0 is specified by the user.

[36] 2. The (x_0,y_0) couple is obtained by generating randomly two real numbers following a uniform distribution over a specified Δx and Δy range.

[37] In addition to this starting position, each photon is assigned a unit-vector displacement defined by:

$$\vec{V} = \begin{pmatrix} \sin e \cos a \\ \sin e \sin a \\ \cos e \end{pmatrix} \quad (2)$$

with e the elevation and a the azimuth as defined on Figure 5.

2.3.2. Photons Path Algorithm Within the Sample

[38] 1. The first step consists of determining what grid box the photon will reach, knowing its starting position and the displacement vector unit;

[39] 2. if the grid box that is reached is empty, the photon keeps moving in the same direction until it reaches a new grid box. We then return to step 1) ;

[40] 3. if the grid box is occupied by a grain, we determine if the photon is going to interact or not with this grain. We thus calculate the shortest distance D_{short} between the center of the grain and the photon trajectory. If that distance meets the following requirement:

$$D_{\text{short}} < D_{\text{grain}}^{\text{eff}} \quad (3)$$

then the photon interacts with the grain. Otherwise, the photon keeps moving in the same direction until it reaches another grid bow that is not occupied by the same grain. The determination of $D_{\text{grain}}^{\text{eff}}$ is detailed in section 2.3.3.

[41] 4. if the photon interacts with the grain, we determine if the photon is absorbed or scattered. A random real number between 0 and 1 is generated following a uniform distribution: if this number is lower than the single scattering albedo of the grain, the photon is scattered. Otherwise, the photon is absorbed;

[42] 5. if the photon is scattered, a new unit-vector displacement is generated, as a function of the grain phase function, as well as a grain exit position (see section 2.3.3). We then determine the next grid box that is not occupied by the same grain and go back to step 1).

[43] We keep using this algorithm until all photons are absorbed or exit the sample.

2.3.3. Model Assumptions

2.3.3.1. Interaction of a Photon With a Grain and Porosity

[44] As described in the previous section, a photon entering a new grid box that is occupied can either interact with the grain or continue in its original direction. To decide if the

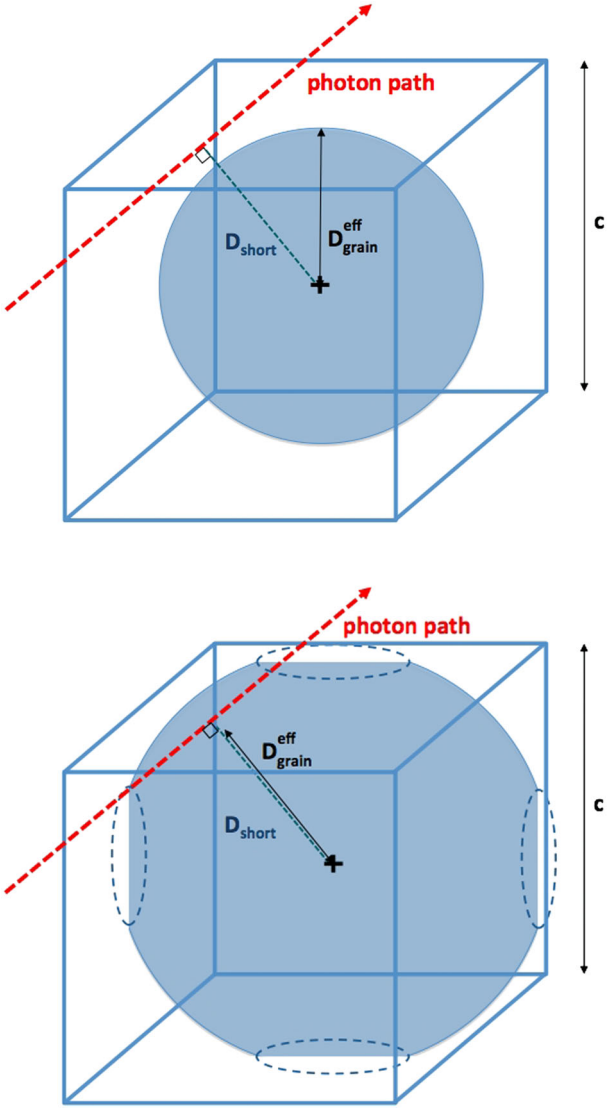

Figure 6. Illustration of the way it is determined if the photon interacts with the grain, in case the porosity is (top) greater than 0.47 and (bottom) less than 0.47.

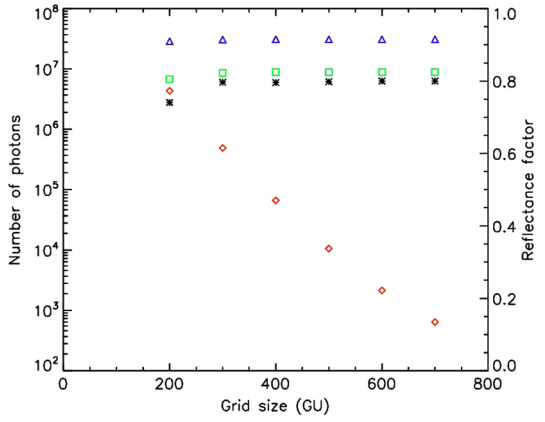

Figure 7. Evolution of the number of photons that exit the sample (blue triangles), are lost (red diamonds) or absorbed (green squares) with the grid size for an number of incident photons of 4.10^7. The grains scattering albedo is set to 0.99. For each grid, the illuminated area is a 200 × 200 GU zone at the center of the sample. The incidence of the incoming beam is 45°. The grain size distribution follows a r^{-3} power law. An isotropic phase function is used here, as well as a porosity of 0.3. The reflectance factor computed at nadir is also indicated on the figure (black stars). We can notice that very quickly the reflectance factor converges.

photon will interact or not with the grain, equation (3) has to be tested by calculating the shortest distance between the center of the grain and the photon trajectory: D_{short}. A simple way of representing the grain is to use a spherical shape centered at the same location that the square shape where the grain is located. To account for the porosity, the diameter of this sphere can be tuned so that the ratio of the volume occupied by the sphere and the volume of the square shape is equal to $1 - p$, where p is the porosity (Figure 6). However, this means that porosity can never be lower than 0.47 (when the diameter of the sphere is equal to the square side). Thus, to simulate lower porosities, we use a new shape that is defined by:

$$d = \text{minimum}(a, b) \tag{4}$$

where a is the distance between the center of the grain (center of the cube where the grain fits) and the square shape, and b is the distance between the center of the grain and a sphere with a diameter larger than the square side (Figure 6). Thus, the porosity can reach 0 in case the diameter of the sphere is equal to $\sqrt{2}c$, with c the square side.

[45] The effect of porosity on the reflectance factor will be discussed in section 3.3.

2.3.3.2. Issue of a Photon-Grain Interaction

[46] Photons that interact with a grain may be either absorbed or scattered. In this latter case, the first step is to determine the new direction of the photon: a random number between 0 and 1 is generated following a uniform distribution and associated with a scattering angle using the cumulative distribution function, as can be seen in Figure 4.

[47] The second step is to determine the position where the photon exits the grain. Assuming that the photon is scattered in a given direction that corresponds to a new unit-vector displacement $\vec{V}_{new}$, we consider the grain cross-section as a disk that is orthogonal to $\vec{V}_{new}$. Assuming that the probability distribution is uniform on the disk, a position on this disk is generated and then projected along the photon direction on a spherical shape that represents the grain, thus leading to a 3-D (x,y,z) position. We only consider here the semisphere whose orientation is in the same direction as $\vec{V}_{new}$. The diameter of the disk that is used to generate the exit position of the photon is equal to the one of the spherical shape described in the previous paragraph if $p > 0.47$, and equal to the square side c for lower porosities.

2.3.4. Model Outputs

[48] At the end of the calculations presented in the previous section, the photons have either been absorbed or have exited the sample. Photons that emerge from the same side as the one they entered are sorted according to the position (x,y) where they cross the plane $z = 0$, and according to their angle of emergence and azimuth. Photons that have emerged through a different side that the one they entered are considered lost. The grid size is discussed in section 3.2.

[49] The reflectance factor and the albedo are then computed following the method developed in *Vincendon et al.* [2007] at different scales: from the unit grid step (see Figures 15 and 16) to the whole illuminated area on the sample. The reflectance factor can be expressed as:

$$R(i, e, \phi) = \frac{r(i, e, \phi)}{\mu_0}\pi \tag{5}$$

with r the bidirectional reflectance and μ_0 the cosine of the incidence angle, i the incidence angle, e the emergence angle, and ϕ the phase angle. It can be computed for different emergence/azimuth angles by summing the number of photons that exit the sample following a $\pm\alpha°$ cone around the emergence angle.

3. Model Validation Tests

3.1. Introduction

[50] In order to validate the global behavior of the model, the reflectance factor is computed for a wide range of geometric conditions and grains parameters. Results are then compared to *Douté and Schmitt* [1998] that themselves compared their results to *Hapke* [1993] as well as a typical adding-doubling model that was used as a reference [*de Haan et al.*, 1987]. Phase functions, as well as single scattering albedos, illumination and emergence angles are chosen to compare the results with the one presented in *Douté and Schmitt* [1998]. These tests are performed using a one lobe Henyey-Greenstein phase function. Both back ($g < 0$) and forward ($g > 0$) scattering media are considered within a physically realistic range of values ($-0.5 \leq g \leq 0.8$, see Figure 4). The elevation angle θ_0 of the incoming beam is set to an intermediate value of 45°. The reflectance factor is calculated for emergence angles lying between –85° and 85° by increments of 5° in the source azimuthal plane ($\phi = 0°$) and in the antisource one ($\phi = 180°$). All the grains are set with the same single scattering albedo ω that ranges from 0.2 to 0.99. A porosity of 0.3 is used for these tests. The influence of this parameter is discussed in section 3.3.

3.2. Grid Size

[51] Photons that have emerged through a different side that the one they entered are considered lost. The grid that

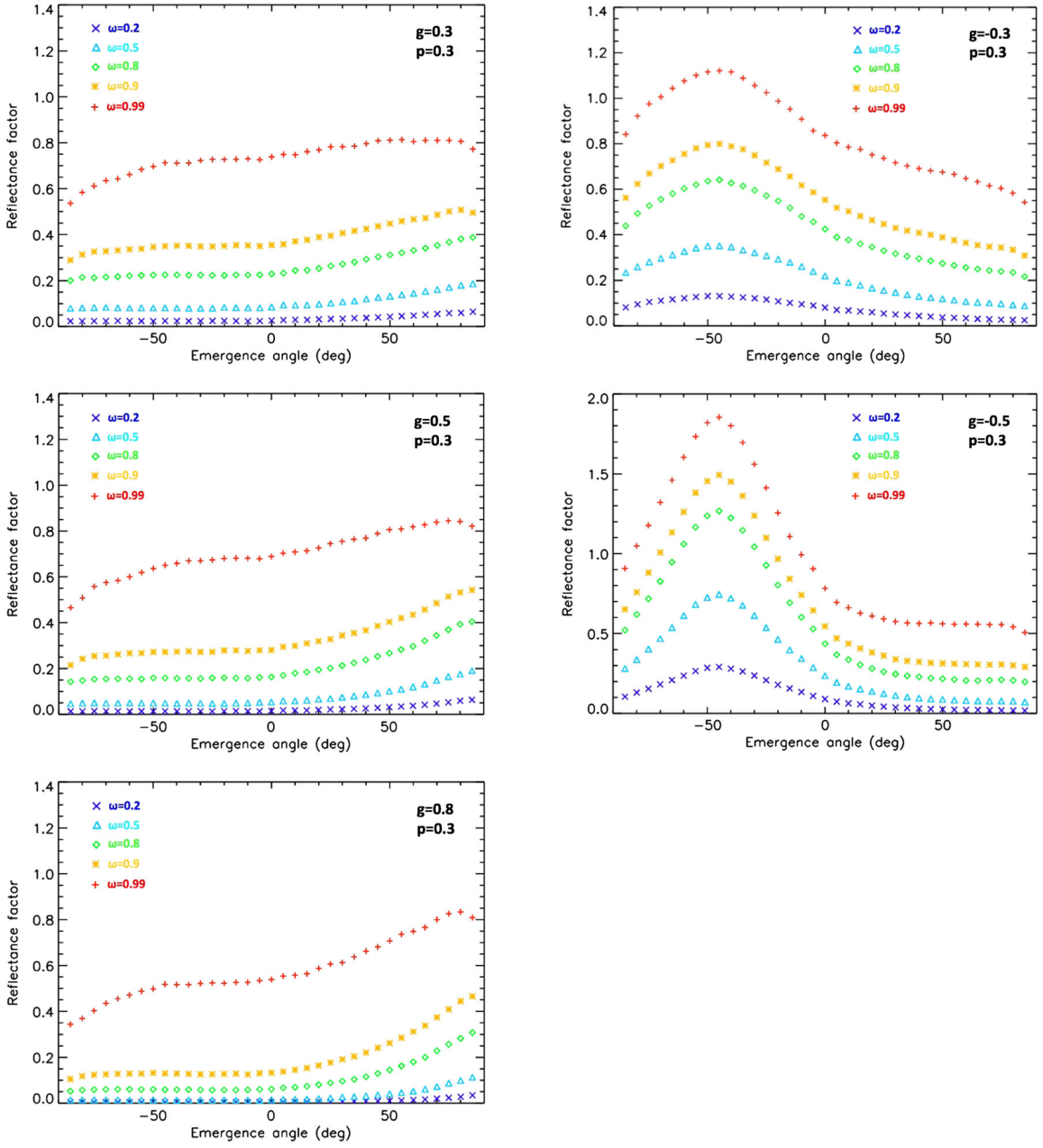

Figure 8. Evolution of the reflectance factor with the emergence angle for different forward and backward scattering media and single scattering albedos assuming a porosity of 0.3. The incidence of the incoming beam is 45°. The reflectance factor is computed over a solid angle defined by a 4° cone. All samples follow a r^{-3} power law granulometric distribution.

is used in the simulations should therefore be large enough to be considered as infinite for the photons, so that at the end the number of the photons that are lost is small, and their impact negligible, as illustrated in Figure 7. In what follows, we consider a 700 × 700 × 300 GU grid that meets this requirement.

3.3. Results

[52] For a lambertian surface, the evolution of the number of measured photons with the emergence angle follows the following law:

$$N(e) = A\cos(e)\sin(e) \quad (6)$$

with A an integer. The evolution of the reflectance factor with the emergence angle quantifies the discrepancy between the behavior of a given sample and a lambertian surface.

[53] Figure 8 shows the reflectance factor for the previously defined samples. As the single scattering albedo increases, fewer photons are absorbed and the reflectance factor increases. For forward scattering media ($g > 0$), we can notice that the reflectance factor for low to moderate emergence angles tends to decrease with increasing g, while the opposite behavior is observed at high emergence angle in the antisource direction. The contrast between reflectance factors at low to moderate emergence angle and at high

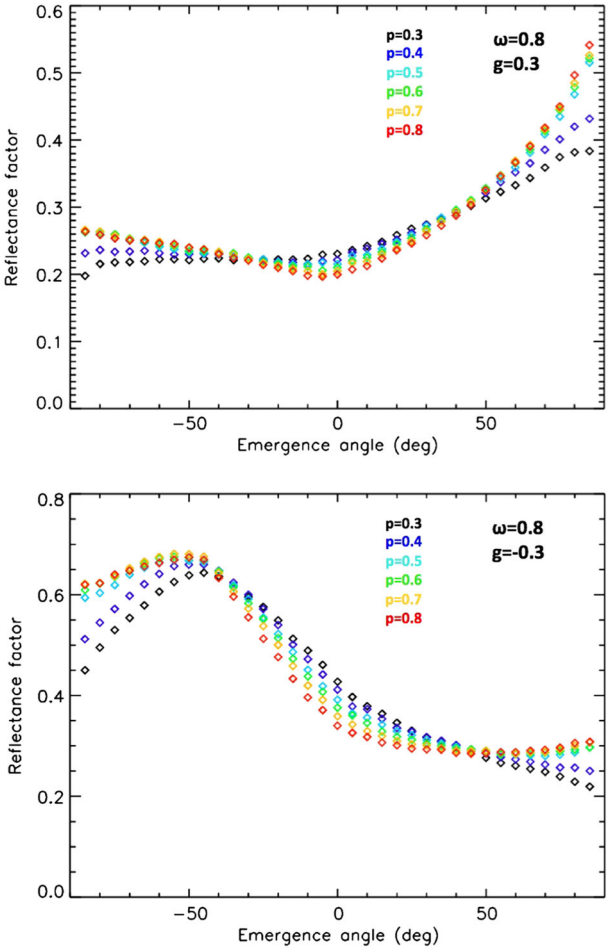

Figure 9. Evolution of the reflectance factor with the emergence angle for different porosities. (top) $g = 0.3$ and $\omega = 0.8$; (bottom) $g = -0.3$ and $\omega = 0.8$. The incidence of the incoming beam is 45°. The reflectance factor is computed over a solid angle defined by a 4° cone.

emergence angle in the antisource direction tends to increase as the asymmetry factor increases. For backward scattering media, the reflectance factor tends to increase in the source direction.

[54] The agreement between these results and the one shown in *Douté and Schmitt* [1998] (and more especially results produced by the *de Haan et al.* [1987] model that serves as a reference), are generally good, both qualitatively and quantitatively (see Figure 8 and Figure 3–5 of *Douté and Schmitt* [1998]).

[55] For forward scattering media ($g > 0$), the agreement is very good from –45° to 45°: the difference with *de Haan et al.* [1987] is less than 3% (in absolute) for $\omega \leq 0.9$ and less than 8% for $\omega = 0.99$). For emergence angles higher than 45°, the reflectance factor increase in the antisource direction tends to be smoother in our simulations. However, as the anisotropy of the phase function increases ($g = 0.5$ and $g = 0.8$), the agreement between our model and the other models tends to increase at high emergence angle. It should be noted that whereas *Hapke* [1993] and *Douté and Schmitt* [1998] models cannot reproduce the results of *de Haan et al.* [1987] for highly forward scattering media ($g = 0.8$) (see Figure 5 of *Douté and Schmitt* [1998]), especially as the single scattering albedo increases, the agreement with our model is very good (the difference is less than 3% for emergence angles from –80 to 50° and less than 8% elsewhere). This can be explained by the fact that all multiscattering orders are being modeled here without assumptions, contrary to *Douté and Schmitt* [1998] and *Hapke* [1993].

[56] Figure 9 shows that the behavior of the reflectance factor at high emergence angle highly depends on the porosity. As shown by Figure 6, a high porosity allows the photons that have a high emergence angle to escape more easily, as the probability to encounter a grain before reaching the surface is reduced (for a given single scattering albedo). When the anisotropy of the phase function is moderate ($g = 0.3$), the increase of the number of photons that exit the sample with a high emergence angle (compared to the isotropic case) is limited and the effect of porosity will dominate in the results.

[57] For backward scattering media, the agreement is also qualitatively good from –45° to 45°. However, the reflectance factor that is obtained is higher that the one from other models. This is especially true for the backward scattering lobe (up to 8% for $g = -0.3$ and up to 25% for $g = -0.5$). The difference at nadir is, however, generally within a few percent. As for the forward scattering media, differences for the highest emergence angles can be explained by porosity as can be seen on Figure 9.

[58] The reflectance factor between –45° and 45° globally decreases as the porosity increases, which is consistent with *Hapke* [2008] and *Peltoniemi and Lumme* [1992]. Indeed, as the porosity increases, it becomes more difficult for the photons to penetrate deep into the sample and most of the interactions occur in the top layers. However, the reflectance factor tends to decrease when the porosity increases at high emergence angle. This result comes directly from the fact that we do not simulate surface roughness: The top of all grains on the surface are aligned. Thus, for low porosity, only the photons which escape the grains close enough to

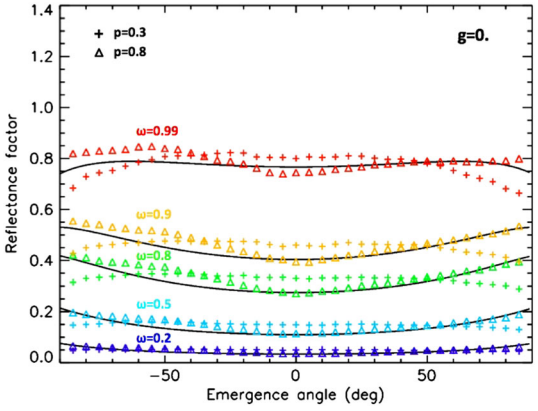

Figure 10. Evolution of the reflectance factor with the emergence angle for a sample composed of isotropic scattering grains. Two porosities are tested: p = 0.3 (crosses) and p = 0.8 (triangles). The incidence of the incoming beam is 45°. The reflectance factor is computed over a solid angle defined by a 4° cone. The angular curves given by *Hapke* [1993] (approximate solution) have been added for comparison (black continuous lines).

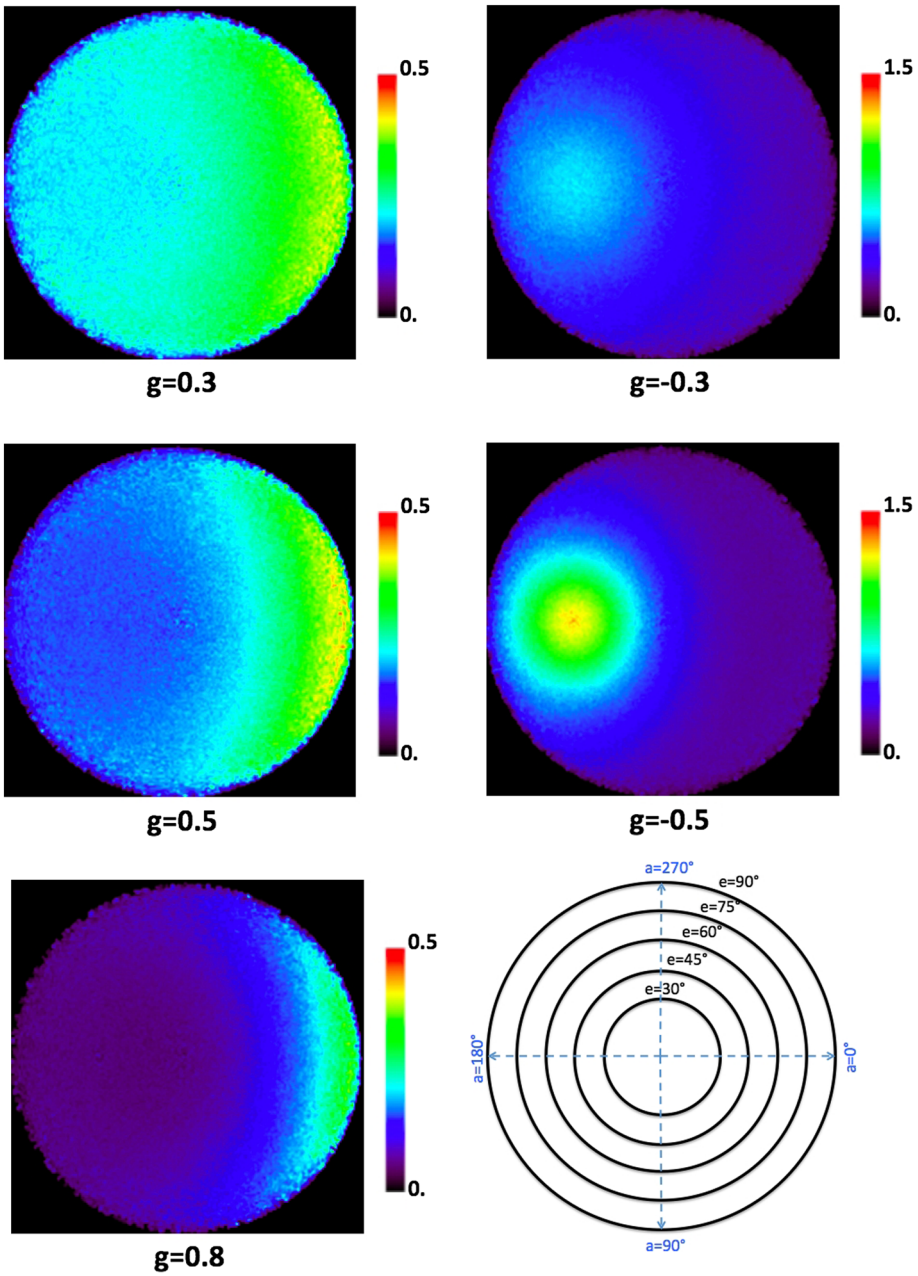

Figure 11. Spatial evolution (emergence and azimuth) of the reflectance factor for different forward and backward scattering media assuming a single scattering albedo of 0.8 and a porosity of 0.3. Emergence angle is radial from the center of the plot, 0 at center, and 90 at perimeter. Azimuth angle is clockwise from far right. All samples follow a r^{-3} power law granulometric distribution. The light comes from the left (so their azimuth is equal to 0°), with an incidence angle of 45°.

the surface can exit the sample with a high emergence angle (Figure 6). Surface roughness however plays an important role at high emergence angle and should be simulated in the future to evaluate the impact of porosity at high emergence angle.

[59] The same tests were performed for a sample composed of isotropic scattering grains ($g = 0$). *Hapke* [1993] derived a simple analytical expression for the isotropic case by using the two-stream approximation:

$$R(\mu_0, \mu) = \frac{\omega}{4\pi^2} \frac{\mu_0}{\mu_0 + \mu} \frac{1 + 2\mu_0}{1 + 2\gamma\mu_0} \frac{1 + 2\mu}{1 + 2\gamma\mu} \quad (7)$$

with R the reflectance factor, ω the single scattering albedo, $\gamma = \sqrt{1 - \omega}$, μ_0 the cosine of the incidence angle, and μ the cosine of the emergence angle.

[60] Figure 10 shows that the agreement is very good between our results and the one provided by the approximate solution from *Hapke* [1993]. As for previous results, the agreement is better for low porosities: the difference is less that about 5%, for all emergence angles and single scattering albedos.

[61] Interestingly, a small increase of the reflectance factor occurs for low phase angles, which highlights the opposition effect (SHOE), and whose amplitude increases with

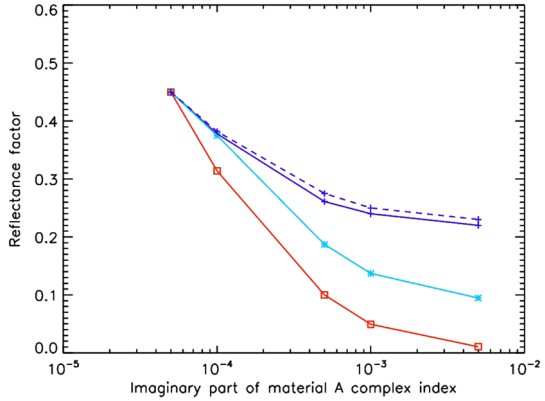

Figure 12. Evolution of the reflectance factor at 1 μm of various mixtures made of two materials (A and B) with the imaginary part of the complex optical index of one of the materials (material A). Crosses (continuous dark blue line): 50%-50% spatial mixture, with the boundary between both materials that is parallel to the source direction; stars (light blue): 50%-50% intimate mixture. The reflectance factor of a homogeneous sample only made of material A following the same lognormal granulometric distribution as previously (red squares) and of a ideal 50%-50% spatial mixture (crosses, dashed blue line) have been added for comparison.

the porosity, as described in *Hapke* [1993] and *Stankevich et al.* [1999]. Its amplitude, however remains quite small (5 to 15% in relative) as well as its angular width remains large (half-width of the peak around 10 – 15°). These results come directly from the rather large granulometric distribution (r^{-3} with the ration of the smallest to the largest grain size set to 20) but also from the spatial law distribution of the photons escaping the grains (see section 2.3.3) which makes the photons generally escape the grain at a considerable distance from their entry point, thus limiting the SHOE amplitude. Note that this effect is not taken into account in the approximate solution from *Hapke* [1993].

[62] Emergence/azimuth diagrams of the reflectance factor can also be derived from our model (e.g., Figure 11), thus allowing comparisons with photometric measurements of planetary bodies and laboratory measurements of various representative samples. One major concern in photometric remote sensing data is the limited number of observations for a same location, and thus, a limited range of covered geometries, which might lead to misinterpretation. Emergence/azimuth diagrams as those shown in Figure 11 are therefore particularly interesting to investigate the extension of characteristic photometric features over the emergence/azimuth ranges. For forward scattering media ($g > 0$), we can see on Figure 11 that the extension of the forward scattering peak tends to reduce as the asymmetry parameter g increases (confirming the trend on Figure 8), what makes it more difficult to detect. However, for backward scattering media ($g < 0$), as the asymmetry factor decreases, the intensity of the backward scattering peak increases as well as its extension, what makes it easier to detect. This could explain why the remote sensing observations are more sensitive to backscattering than to forward scattering.

4. First Applications

4.1. Complex Mixtures

[63] Different kinds of mixtures can be easily implemented in the model, like spatial mixtures (a majority of photons only interact with material A or material B), intimate mixtures (a majority of photons interacts with both materials) and layered mixtures where a layer of material A covers a material B.

[64] It is generally admitted that the smaller grains, as well as the most absorbing grains will determine the global photometric behavior of the sample [*Nash and Conel*, 1974; *Singer*, 1981; *Clark*, 1983]. We generate here a sample made of two materials: material A and material B, material A having a complex optical index n_A(n_A = 1.4 + ik, with k that varies between 5.10^{-5} and 5.10^{-3}) and material B having a complex optical index n_B (n_A = 1.4+5.10^{-5}i). These indexes are common values for minerals in the NIR. Then four different mixtures are tested:

[65] 1. a 50-50% spatial mixture. For both materials, the granulometric distribution follows a lognormal law whose maximum is reached at 8 GU (80 μm with 1 GU = 10 μm).

[66] 2. a 50-50% intimate mixture with the same materials A and B used previously.

[67] 3. a mixture made of a layer of fine grained material B (1 GU) on top of a sample made of material A. The granulometric distribution of material A follows a lognormal law whose maximum is reached at 8 GU (80 μm with 1 GU = 10 μm).

[68] 4. a mixture made of a layer of fine grained material A (1 GU) on top of a sample made of material B. The granulometric distribution of material B follows a lognormal law whose maximum is reached at 8 GU (80 μm with 1 GU = 10 μm).

[69] For all grains, a one lobe Henyey-Greenstein phase function with g = 0.3 is used. Then the radiative transfer code is run to compute the reflectance factor for an incidence angle of 45° and an emergence angle of 0° (nadir) at the wavelength of 1 μm .

[70] Results (see Figure 12) show that as one of the material of the intimate mixture becomes more and more absorbent, the reflectance factor decreases making the other

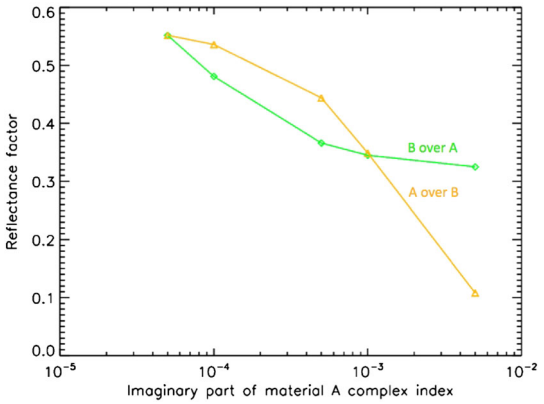

Figure 13. Same as Figure 12. Diamonds (green): a thin layer of (bright) material B covering a sample made of material A; triangles (orange): a thin layer of material A covering a sample made of (bright) material B.

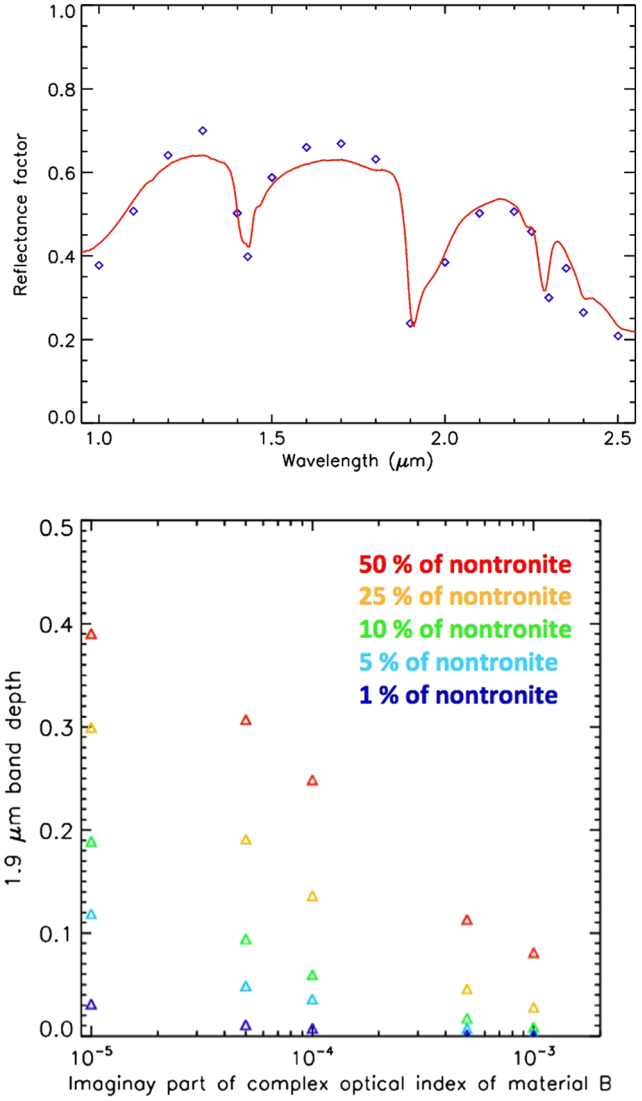

Figure 14. (top) Reflectance spectrum of a nontronite from Reflectance Experiment Laboratory (RELAB) database (continuous red line) and modeling results (blue diamonds). The nontronite sample has been sieved so that the grain size is between 45 and 75 μm. Illumination is set at 30° and detector is set at nadir. For the simulations, the sample grain size distribution is a lognormal law centered at 60 μm and the complex optical index is taken from *Poulet et al.* [2008]. A 2-lobe Henyey-Greenstein phase function is used with $b = 0.4$ and $c = -0.6$ [*Shepard and Helfenstein*, 2007]. The difference between the reference spectrum and the modeling results are within ~5% and due to possible differences between the optical index of the samples in *Poulet et al.* [2008] and the one from RELAB database. (bottom) Evolution of the 1.9 μm absolute band depth when the nontronite sample is mixed with a second sample (assumed to have the same grain size distribution).

(bright) material contribution less and less important. However, when considering a spatial mixture, most of the photons only encounter one of the two materials, which limits in theory the reflectance factor decrease to the average of the reflectance factor of a sample made of material A and a sample made of material B. However, in our simulations, the sample that is used is rather small (700 × 700 × 300 GU, with a 300 × 300 GU surface that is illuminated), and the imaginary part of the complex optical index may be also rather low (down to 5.10^{-5}). Therefore, the fraction of the photons that encounter both materials might not be negligible: by decreasing the imaginary part of the optical index of material A, the global reflectance factor can be lower than the one in the case of an ideal spatial mixture.

[71] In the case of a thin layer of material B (10 μm of grain size) covering a sample made of material A, we can notice that as the imaginary part of the optical index of material A increases, the reflectance factor decreases first rather quickly and then more slowly as it becomes less and less sensitive to the optical properties of the underlying material (Figure 13). However, when material A covers a sample made of material B, the reflectance factor first decreases rather slowly as the single scattering albedo of such small grains is not very sensitive at first to the increase of the imaginary part of the optical index. As the imaginary part of the optical index of the covering layer keeps increasing, more and more photons are absorbed by this layer and the reflectance factor becomes less and less sensitive to the properties of the underlying material.

[72] The model can thus be used to compute the radiative transfer within particulate mixtures and study for example the detectability of specific compounds among others. To illustrate this, the reflectance spectrum of nontronite has been computed at specific wavelengths and then compared

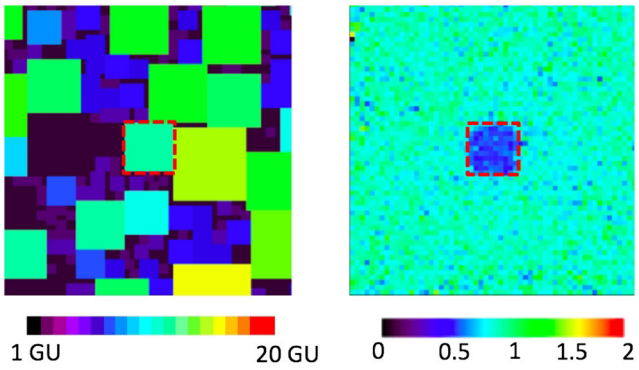

Figure 15. (left) Top layer granulometric distribution of the illuminated zone of a sample made of material A and a grain of material B (identified by dashed red line). (right) Material B exhibits an absorption band at 1.9 μm, whereas material A does not. The ratio of reflectance factor maps obtained at 1.8 μm (no absorption for A and B) and 1.9 μm (absorption for B), is represented. This ratio corresponds to 1 – BD, with BD the relative band depth. The first simulation is run at 1.9 μm, where material B is set with nontronite optical index at 1.9 μm ($n_B = r_{abs} + i\, k_{abs}$, with $r_{abs} = 1.40$ and $k_{abs} = 4.6 \times 10^{-4}$). Material A is set with nontronite optical index at 1.8 μm where nontronite does not exhibit any absorption band, in order to simulate the continuum ($n_A = r_{cont} + i\, k_{cont}$, with $r_{cont} = 1.40$ and $k_{cont} = 2.78 \times 10^{-5}$). The second simulation is run where both materials A and B are set with nontronite optical index at 1.8μm. The incidence light beam comes from the left, with an incidence angle of 45°.

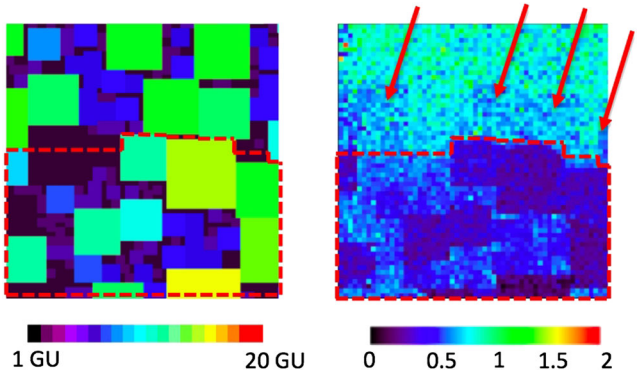

Figure 16. (left) Top layer granulometric distribution of the illuminated zone of a spatial mixture made of materials A and B (identified by dashed red line). (right) Ratioed reflectance factors for the same conditions of simulation as on Figure 15.

to actual lab data (Figure 14, top). The optical constants of nontronite have been obtained from *Poulet et al.* [2008] and the phase function is taken from *Shepard and Helfenstein* [2007]. The fit is quite good even if small differences (within ~5%) can be noted. These differences are most likely due to the uncertainty on the optical index which was derived from a different sample than the one whose reflectance spectrum was measured. The 1.9 μm absolute band depth (defined here as the reflectance difference between 1.8 and 1.9 μm) is 0.41 for a sample made of pure nontronite (grain size between 45 and 75 μm). As expected, Figure 14 (bottom) shows that this band depth decreases quickly as the second material becomes more absorbent. Interestingly, we can notice than when the nontronite is mixed with a very transparent material ($k = 10^{-5}$), the band depth remains quite high for various fractions of nontronite. With 50% of nontronite, the 1.9 μm band depth (0.39) remains very close from the one of a pure sample (0.41). With only 5% of nontronite, the band depth remains at 0.12. Nontronite mixed with bright material therefore remains easy to detect compared to the case where it is mixed with dark material ($k = 10^{-3}$), where the band depth is below 1% for a nontronite fraction of 10%, thus close to the detection level.

4.2. Multi-Scale Surveys

[73] The model also allows us to study the evolution of the reflectance factor of samples at different scales: from the grain scale to the macroscopic scale. As an example, we generate a sample made of a material A, to which is added a grain composed of a material B. The whole sample follows a power law granulometric distribution (r^{-3}). The grain made of material B is a 100 μm grain situated on top of the sample, bordered by grains made of material A. For this simulation, we use the optical constants of nontronite from *Poulet et al.* [2008]. A first simulation is run at 1.9 μm where nontronite exhibits a deep absorption band due to the structural water. Material B is set with nontronite optical index at 1.9 μm ($n_B = r_{abs} + i\, k_{abs}$, with $r_{abs} = 1.40$ and $k_{abs} = 4.6 \times 10^{-4}$). Material A is set with nontronite optical index at 1.8 μm where nontronite does not exhibit any absorption band, in order to simulate the continuum ($n_A = r_{cont} + i\, k_{cont}$, with $r_{cont} = 1.40$ and $k_{cont} = 2.78 \times 10^{-5}$). A second simulation is then run where both material A and B are set with nontronite optical index at 1.8 μm.

[74] The reflectance factor is then computed at the pixel scale (1 GU). By ratioing the reflectance factors obtained in both simulations, the 1.9 μm band absorption depth can be mapped, as can be seen on Figure 15. The grain, made of material B, can be clearly identified in the middle of the sample. The spectral signature of nontronite seems limited to the grain itself and no clear increase of the nontronite spectral signature can be identified on neighboring grains: the effect of multiple scattering is below the noise level, thus lower than about 8% in relative, or 5% in absolute (1 σ level).

[75] A second set of simulations is then run by generating a spatial mixture made of the same materials as the one

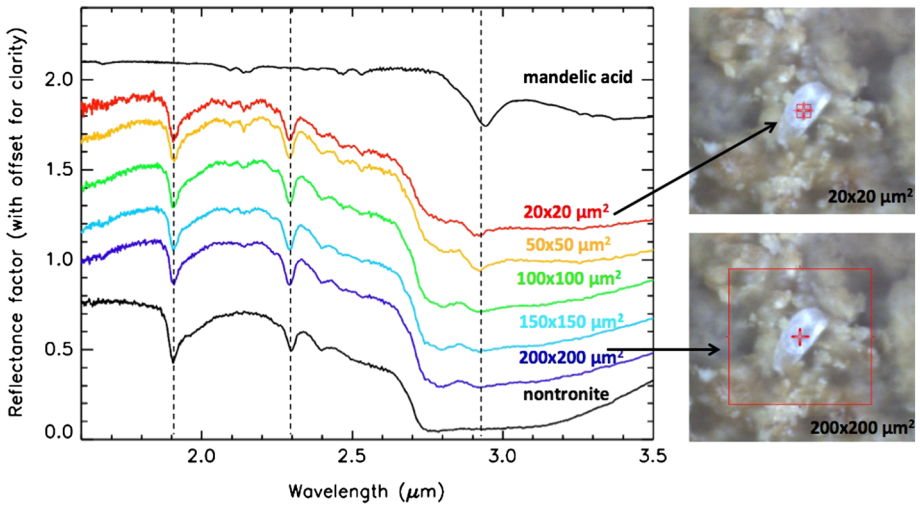

Figure 17. Evolution of the reflectance spectra of a spot looking at a grain made of mandelic acid, surrounded by nontronite grains. The spectra were acquired with a iN10 Nicolet IR microscope. The spot size ranges from 20 × 20 μm^2 to 200 × 200 μm^2.

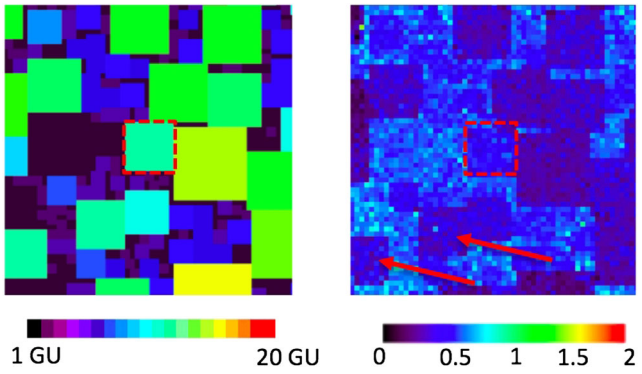

Figure 18. (left) Top layer granulometric distribution of the illuminated zone of a sample made of material B and a grain of material A (identified by dashed red line). (right) Ratioed reflectance factors for the same conditions of simulation as on Figure 15.

of the previous set of simulations: 50% of material A and 50% of material B. Contrary to the case of an isolated grain made of material B, the effect of multiple scattering on the reflectance factor can be clearly seen here (Figure 16): grains close to the boundary between both materials and made of material A also exhibit a 1.9 μm band absorption (pointed by red arrows on Figure 16). Indeed, more absorbing grains (made of material B) are present and photons that are scattered close to the boundary between both materials have a much higher probability to interact with these grains (and thus to be absorbed), compared to the previous case. We can also notice the weak absorption of the smaller grains made of material B: for the smaller grains the increase of the imaginary part of their optical index has little effect on their single scattering albedo.

[76] This kind of simulation is important to better understand the radiative transfer at the grain scale, and therefore, to better interpret the data. To illustrate this, we prepared different samples, all made of nontronite and whose grain size is smaller than 100 μm, to which have been added a few grains of a second material. These samples are then analyzed with an iN10 Nicolet IR microscope that allows to measure reflectance spectra in the IR from 20×20 to 200×200 μm^2 spots. Here we measure the reflectance spectra from a spot that covers a grain of mandelic acid (about 80 μm in size) surrounded by nontronite grains, with different spot sizes, from 200×200 μm^2 to 20×20 μm^2. Figure 17 shows the evolution of the reflectance spectra as the spot size decreases, and we can notice that the nontronite spectral signature is always present in the spectra, even if the mandelic acid spectral features tend to become stronger as the spot size decreases. This trend was also observed in the case of bright grains (other organic compounds but also calcite, surrounded by nontronite).

[77] To better understand these results, we ran a third set of simulations. A grain with no absorption at 1.9 μm (material A) was set at the top of the sample surrounded by grains made of nontronite with a 1.9 μm band (material B). The optical index of mandelic acid is unknown (but smaller than the one of nontronite at 1.8 and 1.9 μm); thus, we set the optical index of the grain made of material A to the optical index of nontronite at 1.8 μm, which is a maximum. As can be seen on Figure 18, we obtain the same kind of behavior as what was observed in the experiments. The 1.9 μm absorption band, almost as strong as for grains made of material B of the same size, is also present where the grain made of material A is set.

[78] As the identification of the different phases at the grain scale and their relationship is critical to assess the climate and geological history of the parent body, modeling results will be essential in the interpretation of grain scale measurements.

5. Conclusion

[79] Most of the models currently used to simulate spectroscopic and photometric behaviors of planetary surfaces consider semi-infinite media. The model presented here allows the consideration of spatially resolved heterogeneities and thus the ability to study the light scattering from the macroscopic to the microscopic scale. Its photometric behavior has been validated by comparing results with *Hapke* [1993], *Douté and Schmitt* [1998], and *de Haan et al.* [1987] for a broad range of geometries and grain physical parameters. A few examples of applications have been presented. In particular, the effect of mixtures structure (spatial, intimate, layered) on the light scattering has been highlighted, in agreement with previous studies. First results also emphasize the importance of multiple scattering at the grain level, which should be taken into account when interpreting such data.

[80] The next step is to use this model to increase our understanding of light scattering in complex media, both at the macroscopic and microscopic scales. Future work will include a systematic survey of different kind of mixtures (spatial, intimate, and layered) for different sets of parameters, including optical properties, phase functions, and grain size distributions. In particular, future work will include to better understand the variation of the phase function with regards to grain size, optical index, roughness, shape, and porosity to derive simple laws that could be implemented in the model. To improve the model's capability to simulate samples made of highly transparent grains, as is the case for ice studies, for example, where very large samples are needed, we also plan to implement a cyclic scheme as in *Shkuratov and Grynko* [2005]. These results will help improving the fast-computing codes that use a semi-infinite approach.

[81] Future work should also allow us to better understand to what extend can spectral signatures be identified at different scales, depending on optical properties, phase functions, and grain sizes. This will allow us to afinate our understanding of remote sensing data of planetary surfaces (like OMEGA (Observatoire pour la Minéralogie, l'Eau, les Glaces, et l'Activité), CRISM (Compact Reconnaissance Imaging Spectrometer for Mars), and VIRTIS (Visible and Infrared Thermal Imaging Spectrometer) data sets, assuming semi-infinite media), as well as future measurements of hyperspectral microscopes such as CIVA-M/I (Comet nucleus Infrared and Visible Analyzer) on-board Rosetta, MicrOmega Mascot on-board Hayabusa-2 or MicrOmega on-board ExoMars missions, which may be able to resolve spatial compositional heterogeneities within a given sample [*Pilorget and Bibring*, 2013].

[82] **Acknowledgments.** The authors would like to thank S. Douté for useful discussions about this work. We are also grateful to C.S Edwards for helping with the manuscript, as well as our colleagues at IAS and Caltech for inspiration and advice. Finally, we thank Y. Shkuratov and an anonymous reviewer for their reviews that helped improving the manuscript.

References

Bottlinger, M., and H. Umhauer (1991), Modeling of light scattering by irregularly shaped particles using a ray-tracing method, *Appl. Opt.*, *30*, 4732–4738, doi:10.1364/AO.30.004732.

Clark, R. N. (1983), Spectral properties of mixtures of montmorillonite and dark grains—Implications for remote sensing minerals containing chemically and physically adsorbed water, *J. Geophys. Res.*, *88*, 10,635–10,644, doi:10.1029/JB088iB12p10635.

Cruikshank, D. P., and C. M. Dalle Ore (2003), Spectral models of Kuiper belt objects and centaurs, *Earth Moon and Planets*, *92*, 315–330, doi:10.1023/B:MOON.000003194839136.7d.

Cruikshank, D. P., T. C. Owen, C. D. Ore, T. R. Geballe, T. L. Roush, C. de Bergh, S. A. Sandford, F. Poulet, G. K. Benedix, and J. P. Emery (2005), A spectroscopic study of the surfaces of Saturn's large satellites: H_2O ice, tholins, and minor constituents, *Icarus*, *175*, 268–283, doi:10.1016/j.icarus.2004.09.003.

de Haan, J. F., P. B. Bosma, and J. W. Hovenier (1987), The adding method for multiple scattering calculations of polarized light, *Astron. Astrophys.*, *183*, 371–391.

Denevi, B. W., P. G. Lucey, and S. B. Sherman (2008), Radiative transfer modeling of near-infrared spectra of lunar mare soils: Theory and measurement, *J. Geophys. Res.*, *113*, E02003, doi:10.1029/2007JE002929.

Douté, S., and B. Schmitt (1998), A multilayer bidirectional reflectance model for the analysis of planetary surface hyperspectral images at visible and near-infrared wavelengths, *J. Geophys. Res.*, *103*, 31,367–31,390, doi:10.1029/98JE01894.

Goetz, W., et al. (2010), Microscopy analysis of soils at the Phoenix landing site, Mars: Classification of soil particles and description of their optical and magnetic properties, *J. Geophys. Res.*, *115*, E00E22, doi:10.1029/2009JE003437.

Grenfell, T. C. (1991), A radiative transfer model for sea ice with vertical structure variations, *J. Geophys. Res.*, *96*, 16,991–17,001, doi:10.1029/91JC01595.

Grundy, W. M., S. Douté, and B. Schmitt (2000), A Monte Carlo ray-tracing model for scattering and polarization by large particles with complex shapes, *J. Geophys. Res.*, *105*, 29,291–29,314, doi:10.1029/2000JE001276.

Grynko, Y., and Y. Shkuratov (2003), Scattering matrix calculated in geometric optics approximation for semitransparent particles faceted with various shapes, *J. Quant. Spectrosc. Radiat. Transfer*, *78*, 319–340, doi:10.1016/S0022-4073(02)00223-6.

Hapke, B. (1993), *Theory of Refectance and Emittance Spectroscopy*, Cambridge Univ. Press, New York.

Hapke, B. (2008), Bidirectional reflectance spectroscopy. 6. Effects of porosity, *Icarus*, *195*, 918–926, doi:10.1016/j.icarus.2008.01.003.

Hartman, B., and D. Domingue (1998), Scattering of light by individual particles and the implications for models of planetary surfaces, *Icarus*, *131*, 421–448, doi:10.1006/icar.1997.5861.

Hillier, J. K. (1997), Scattering of light by composite particles in a planetary surface, *Icarus*, *130*, 328–335, doi:10.1006/icar.1997.5829.

Hillier, J. K., and B. J. Buratti (2001), Monte Carlo simulations of light Scattering by composite particles in a planetary surface, *Icarus*, *149*, 251–261, doi:10.1006/icar.2000.6500.

Johnson, J. R., and W. M. Grundy (2001), Visible/near-infrared spectra and two-layer modeling of palagonite-coated basalts, *Geophys. Res. Lett.*, *28*, 2101–2104, doi:10.1029/2000GL012669.

McKay, D. S., R. M. Fruland, and G. H. Heiken (1974), Grain size and the evolution of lunar soils, *Lunar and Planetary Science Conference Proceedings, Lunar and Planetary Science Conference Proceedings*, vol. 5, pp. 887–906.

Mishchenko, M. I., L. D. Travis, and A. A. Lacis (2002), *Scattering, Absorption, and Emission of Light by Small Particles*, Cambridge Univ. Press, New York.

Muinonen, K., T. Nousiainen, P. Fast, K. Lumme, and J. Peltoneimi (1996), Light scattering by Gaussian random particles: Ray optics approximation, *J. Quant. Spectrosc. Radiat. Transfer*, *55*, 577–601, doi:10.1016/0022-4073(96)00003-9.

Nash, D. B., and J. E. Conel (1974), Spectral reflectance systematics for mixtures of powdered hypersthene, labradorite, and ilmenite, *J. Geophys. Res.*, *79*, 1615–1621, doi:10.1029/JB079i011p01615.

Peltoniemi, J. I. (1993), Radiative transfer in stochastically inhomogeneous media, *J. Quant. Spectrosc. Radiat. Transfer*, *50*, 655–671, doi:10.1016/0022-4073(93)90033-E.

Peltoniemi, J. I., and K. Lumme (1992), Light scattering by closely packed particulate media, *J. Opt. Soc. Am. A*, *9*, 1320–1326, doi:10.1364/JOSAA.9.001320.

Pilorget, C., and J.-P. Bibring (2013), NIR reflectance hyperspectral microscopy for planetary science: Application to the MicrOmega instrument, *Planet. Space Sci.*, *76*, 42–52, doi:10.1016/j.pss.2012.11.004.

Poulet, F., J. N. Cuzzi, D. P. Cruikshank, T. Roush, and C. M. Dalle Ore (2002), Comparison between the Shkuratov and Hapke scattering theories for solid planetary surfaces: Application to the surface composition of two Centaurs, *Icarus*, *160*, 313–324, doi:10.1006/icar.2002.6970.

Poulet, F., R. E. Arvidson, C. Gomez, R. V. Morris, J.-P. Bibring, Y. Langevin, B. Gondet, and J. Griffes (2008), Mineralogy of Terra Meridiani and western Arabia Terra from OMEGA/MEx and implications for their formation, *Icarus*, *195*, 106–130, doi:10.1016/j.icarus.2007.11.031.

Poulet, F., J.-P. Bibring, Y. Langevin, J. F. Mustard, N. Mangold, M. Vincendon, B. Gondet, P. Pinet, J.-M. Bardintzeff, and B. Platevoet (2009), Quantitative compositional analysis of martian mafic regions using the MEx/OMEGA reflectance data 1. Methodology, uncertainties and examples of application, *Icarus*, *201*, 69–83, doi:10.1016/j.icarus.2008.12.025.

Shepard, M. K., and P. Helfenstein (2007), A test of the Hapke photometric model, *J. Geophys. Res.*, *112*, E03001, doi:10.1029/2005JE002625.

Shepard, M. K., and P. Helfenstein (2011), A laboratory study of the bidirectional reflectance from particulate samples, *Icarus*, *215*, 526–533, doi:10.1016/j.icarus.2011.07.033.

Shkuratov, Y., L. Starukhina, H. Hoffmann, and G. Arnold (1999), A model of spectral albedo of particulate surfaces: Implications for optical properties of the Moon, *Icarus*, *137*, 235–246, doi:10.1006/icar.1998.6035.

Shkuratov, Y., V. Kaydash, V. Korokhin, Y. Velikodsky, D. Petrov, E. Zubko, D. Stankevich, and G. Videen (2012), A critical assessment of the Hapke photometric model, *J. Quant. Spectrosc. Radiat. Transfer*, *113*, 2431–2456, doi:10.1016/j.jqsrt.2012.04.010.

Shkuratov, Y. G., and Y. S. Grynko (2005), Light scattering by media composed of semitransparent particles of different shapes in ray optics approximation: Consequences for spectroscopy, photometry, and polarimetry of planetary regoliths, *Icarus*, *173*, 16–28, doi:10.1016/j.icarus.2003.12.022.

Singer, R. B. (1981), Near-infrared spectral reflectance of mineral mixtures—Systematic combinations of pyroxenes, olivine, and iron oxides, *J. Geophys. Res.*, *86*, 7967–7982, doi:10.1029/JB086iB09p07967.

Stamnes, K., S.-C. Tsay, K. Jayaweera, and W. Wiscombe (1988), Numerically stable algorithm for discrete-ordinate-method radiative transfer in multiple scattering and emitting layered media, *Appl. Opt.*, *27*, 2502–2509.

Stankevich, D., and Y. Shkuratov (2004), Monte Carlo ray-tracing simulation of light scattering in particulate media with optically contrast structure, *J. Quant. Spectrosc. Radiat. Transfer*, *87*, 289–296, doi:10.1016/j.jqsrt.2003.12.014.

Stankevich, D. G., Y. G. Shkuratov, and K. Muinonen (1999), Shadow-hiding effect in inhomogeneous layered particulate media, *J. Quant. Spectrosc. Radiat. Transfer*, *63*, 445–458, doi:10.1016/S0022-4073(99)00030-8.

Vincendon, M., Y. Langevin, F. Poulet, J.-P. Bibring, and B. Gondet (2007), Recovery of surface reflectance spectra and evaluation of the optical depth of aerosols in the near-IR using a Monte Carlo approach: Application to the OMEGA observations of high-latitude regions of Mars, *J. Geophys. Res.*, *112*, E08S13, doi:10.1029/2006JE002845.